


# The role of microstructure in the impact induced temperature rise in hydroxyl terminated polybutadiene (HTPB)–cyclotetramethylene-tetranitramine (HMX) energetic materials using the cohesive finite element method

Cite as: J. Appl. Phys. **128**, 065901 (2020); <https://doi.org/10.1063/5.0011264>  
Submitted: 19 April 2020 . Accepted: 16 July 2020 . Published Online: 10 August 2020

Ayotomi M. Olokun, Chandra Prakash , I. Emre Gunduz, and Vikas Tomar 

## COLLECTIONS

 This paper was selected as Featured



View Online



Export Citation



CrossMark

## ARTICLES YOU MAY BE INTERESTED IN

[Role of dynamical compressive and shear loading on hotspot criticality in RDX via reactive molecular dynamics](#)

Journal of Applied Physics **128**, 065101 (2020); <https://doi.org/10.1063/5.0014461>

[Defects chemistry in high-efficiency and stable perovskite solar cells](#)

Journal of Applied Physics **128**, 060903 (2020); <https://doi.org/10.1063/5.0012384>

[A practical guide for crystal growth of van der Waals layered materials](#)

Journal of Applied Physics **128**, 051101 (2020); <https://doi.org/10.1063/5.0015971>

Lock-in Amplifiers  
up to 600 MHz



# The role of microstructure in the impact induced temperature rise in hydroxyl terminated polybutadiene (HTPB)–cyclotetramethylene-tetranitramine (HMX) energetic materials using the cohesive finite element method

Cite as: J. Appl. Phys. 128, 065901 (2020); doi: 10.1063/5.0011264

Submitted: 19 April 2020 · Accepted: 16 July 2020 ·

Published Online: 10 August 2020



Ayotomi M. Olokun,<sup>1</sup> Chandra Prakash,<sup>1</sup>  I. Emre Gunduz,<sup>2</sup> and Vikas Tomar<sup>1,a)</sup> 

## AFFILIATIONS

<sup>1</sup>School of Aeronautics and Astronautics, Purdue University, West Lafayette, Indiana 47907, USA

<sup>2</sup>Department of Mechanical and Aerospace Engineering, Naval Postgraduate School, Monterey, California 93943, USA

<sup>a)</sup>Author to whom correspondence should be addressed: [tomar@purdue.edu](mailto:tomar@purdue.edu). Telephone: (765)-494-3423

## ABSTRACT

In this work, microstructure dependent impact-induced failure of hydroxyl-terminated polybutadiene (HTPB)–cyclo-tetra-methylene-tetra-nitramine (HMX) energetic material samples is studied using the cohesive finite element method (CFEM). The CFEM model incorporates experimentally measured viscoplastic constitutive behavior, experimentally measured interface level separation properties, and phenomenological temperature increase due to mechanical impact based on viscoplastic and frictional energy dissipation. Nanoscale dynamic impact experiments were used to obtain parameters for a strain-rate dependent power law viscoplastic constitutive model in the case of bulk HTPB and HMX as well as the HTPB–HMX interfaces. An *in situ* mechanical Raman spectroscopy (MRS) setup was used to obtain bilinear cohesive zone model parameters to simulate interface separation. During analyses, the impact-induced viscoplastic energy dissipation and the frictional contact dissipation at the failed HTPB–HMX interfaces is found to have a significant contribution toward local temperature rise. Microstructures having circular HMX particles show a higher local temperature rise as compared to those with diamond or irregularly shaped HMX particles with sharp edges indicating that the specific particle surface area has a higher role in temperature rise than particle shape and sharp edges. Regions within the analyzed microstructures near the HTPB–HMX interfaces with a high-volume fraction of HMX particles were found to have the maximum temperature increase.

Published under license by AIP Publishing. <https://doi.org/10.1063/5.0011264>

## I. INTRODUCTION

Energetic materials (EM) used as polymer-bonded explosives (PBXs)<sup>1</sup> consist of about 60%–95% solid oxidizer material, embedded inside a polymeric binder, e.g., cyclo-tetra-methylene-tetra-nitramine (HMX) embedded in polymer binder [hydroxyl-terminated polybutadiene (HTPB)].<sup>1</sup> Microstructural inhomogeneities in such materials, such as particle clustering, voids, matrix–particle interfaces, etc., can induce “hot spots” due to external environmental stimuli, such as impact, temperature change, etc. Hot spots are regions in an EM’s microstructure that have sufficient size and temperature to start chemical reactions leading to detonation.<sup>1</sup> The complex microstructure

of EMs is a key factor that affects the mechanical and local temperature behavior under impact loading. Understanding the mechanisms that cause the local temperature to rise within an EM microstructure due to impact is an important consideration for the prevention of hot-spot initiation and detonation. Researchers have attempted to identify several mechanisms, such as adiabatic compression, void collapse, crack tip heating, frictional heating, etc., that may be responsible for hot-spot formation.<sup>2</sup> Such mechanisms involve energy dissipation within an EM microstructure due to impact-induced deformation, crack formation, stress wave propagation in bulk material (e.g., matrix, particle), interface (e.g., matrix–particle interface) failure, etc. Three

fundamentally different types of failure mechanisms in an EM microstructure can be induced by impact: particle fracture, particle–binder interfacial failure, and cavitation in the binder. However, often a combination of such failure mechanisms occurs simultaneously.<sup>3</sup> In a typical HTPB–HMX EM, particle size, volume fraction, and the time span necessary to cause initiation of detonation require a detailed investigation.<sup>2</sup> Rae *et al.*<sup>4</sup> have shown experimentally that debonding of particle–binder interfaces in EMs starts around large particles and the resulting crack first propagates along the crystal–binder interfaces. Palmer *et al.*<sup>5</sup> and Rae *et al.*<sup>6</sup> also observed that the crystal–binder interface failure is the dominant cause of crack propagation. Fracture resistance and the strength of EMs have been shown to depend on the interface chemical composition by Prakash *et al.*<sup>7</sup> Drodge and Proud<sup>8</sup> observed that the yield strain of an EM decreases with increase in the energetic particle size. Studies on particle morphology effects on mechanical behavior also show a clear dependence of the response of EMs to particle shape. Work by Liu *et al.*<sup>9</sup> showed that sharper (rod-like) particles have a higher sensitivity to friction and impact than smoother (plate-like) particles.

Numerical techniques based on the finite element method as well as meshfree methods have been used to simulate the failure behavior of a variety of EMs. Cohesive zone models (CZMs) have been used to simulate the interface failure in EMs by several researchers.<sup>10–13</sup> The energetic particle size was found to affect the hardening behavior as well as the debonding behavior by Tan *et al.*<sup>14</sup> Debonding of the interfaces between energetic particle and the binder matrix was shown to be affected by the applied strain rate.<sup>15</sup> Barua and co-workers<sup>10,11,16,17</sup> have used a cohesive finite element method (CFEM) to study the impact behavior of various idealized microstructure of PBXs. However, the numerical and experimental techniques used in literature studies<sup>18–21</sup> to study the deformation behavior of EMs employ experimental property values that are not based on direct local interface based measurements.<sup>22</sup> In this work, experimentally obtained interface level mechanical and failure properties are used to investigate the effect of HMX particle shape and volume fraction on the thermomechanical behavior of HTPB–HMX EM microstructures (HTPB is the binder). For the purposes of this work, *in situ* mechanical Raman spectroscopy (MRS)<sup>7,23</sup> and nanoscale impact experiments<sup>24</sup> are used to obtain the constitutive properties and the separation properties. Impact-induced temperature rise is modeled based on an approach similar to the work of Barua and Zhou.<sup>10</sup> In order to observe the effect of microstructure on the impact-induced failure and the impact-induced local temperature rise behavior, two-dimensional (2D) microstructure samples of HTPB–HMX EMs consisting of different HMX particle shapes and volume fraction are analyzed.

The remaining sections are arranged as follows: Sec. II describes the experimental procedure used. Section III presents the numerical method, the corresponding CFEM model, and the analyzed HTPB–HMX microstructures. Section IV presents results of the simulated impact-induced failure behavior. Section V presents summary and conclusions.

## II. EXPERIMENTAL METHODS

The viscoplastic stress–strain model and bilinear cohesive zone model parameters are obtained using experimental methods explained briefly in this section. These methods have been

**TABLE I.** Viscoplastic material parameters obtained for HMX, HTPB, and HTPB–HMX interface. Reproduced with permission from *Nano-Energetic Materials* (Springer Singapore, 2019), p. 275. Copyright 2019 Springer Nature Singapore Pte Ltd.

Parameter	$\chi$ (MPa) <sup>-n</sup>	m	n
HTPB	0.54	-0.18	1.78
HMX	1.08	-0.79	1.58
HTPB–HMX interface	1.59	-0.87	1.88

established in earlier publications.<sup>7,23,25</sup> In order to create samples, Isophorone Di-Isocyanate (IPDI) is mixed with R-45M liquid polybutadiene at an index ratio of 1.05 to create an HTPB polymer binder. Polycrystalline HMX particles were manually put into the binder, and the mixture was cured in an oven at 60 °C for 10 days. When fully cured, the crystal–binder samples of appropriate particle shapes and sizes were obtained.

A stress–strain–strain-rate power law based constitutive relation was obtained experimentally. Precise impacts, at any selected location within a microstructure, especially at the interfaces, is a novel capability of the nanoscale dynamic impact experimental setup.<sup>23,26</sup> The viscoplastic constitutive model<sup>23</sup> is given by a power law

$$\bar{\epsilon}^{vp} = \chi \left( \frac{\dot{\bar{\epsilon}}^{vp}}{\dot{\bar{\epsilon}}^0} \right)^m (\bar{\sigma})^n. \quad (1)$$

Here, the equivalent stress,  $\bar{\sigma}$ , and effective viscoplastic strain,  $\bar{\epsilon}^{vp}$ , are obtained from the impact experiment.  $\dot{\bar{\epsilon}}^0$  is a reference strain rate assumed to be 1 s<sup>-1</sup>. The experimentally measured stress and strain at different strain rates are then used to obtain the model parameters  $\chi$ ,  $m$ , and  $n$  of Eq. (1) for HTPB, HMX, and HTPB–HMX interface, as shown in Table I.<sup>25</sup>

A CZM is used to simulate local fracture behavior, and the HTPB–HMX interface separation model parameters are obtained using an *in situ* MRS experiment.<sup>7,23</sup> An edge crack tensile specimen is loaded, and the crack tip location is tracked under a microscope. MRS is used to obtain the crack tip stress as the crack propagates. As the crack reaches the interface, the initial stress near the crack tip is taken to be the interface strength and the energy under the corresponding load–displacement curve is taken to be the critical fracture energy. The cohesive zone model parameters for HMX are used as suggested by Barua *et al.*<sup>16</sup> Parameters for HTPB and HTPB–HMX interfaces are measured using experiments reported earlier. Cohesive zone parameters used in this work for HTPB,<sup>23</sup> HMX, and HTPB–HMX interface<sup>7</sup> are given in Table II.

**TABLE II.** Cohesive zone parameters for HTPB, HMX, and HTPB–HMX interface.

Material/interface	Cohesive strength (MPa)	Critical displacement (mm)	Cohesive energy (kJ/m <sup>2</sup> )
HTPB	0.8	0.5	0.2
HMX	100	5 × 10 <sup>-3</sup>	0.25
HTPB–HMX interface	1.6	0.16	0.13

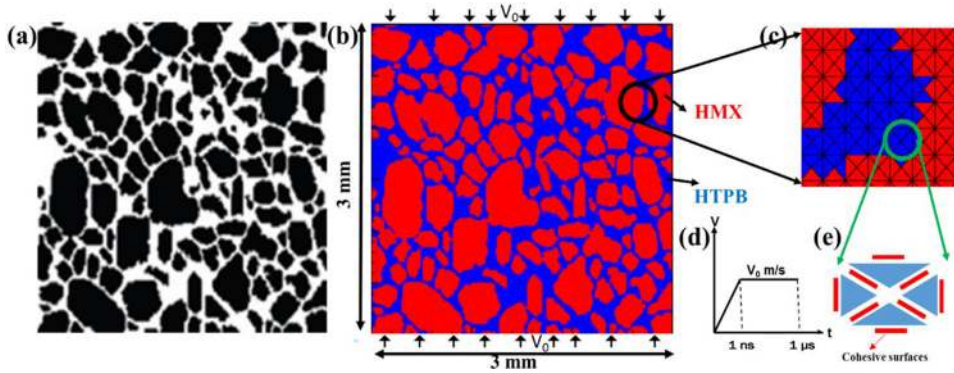


FIG. 1. (a) Digitized microstructure of PBX (Barua *et al.*<sup>16</sup>), (b) corresponding finite element model and boundary conditions, and (c) the mesh details of “cross-triangle,” (d) input velocity profile ( $V_0$  is the input velocity), and (e) cohesive surfaces.

### III. COHESIVE FINITE ELEMENT METHOD

The impact-induced failure behavior of composite materials,<sup>27–29</sup> including energetic materials,<sup>10–12,30</sup> has been simulated previously using CFEM.<sup>31</sup> In this work, a two-dimensional CFEM model of analyzed PBX microstructures with intrinsically specified cohesive surfaces along all bulk finite element boundaries is used to track complex crack patterns.<sup>32</sup> The finite element mesh for the modeled microstructure was generated using the “cross-triangle” elements. Cohesive elements were created by considering all triangle element boundaries as cohesive surfaces, as shown in Fig. 1(c). The element size of  $20\ \mu\text{m}$  with 90 000 triangular elements was selected to be within required convergence bounds established by Tomar *et al.*<sup>33</sup> A Newmark  $\beta$  method based time integration scheme is used. To ensure numerical stability, it is required that the time step and the cohesive separation increment are sufficiently small in each numerical step. The average time step was chosen based on Courant–Freidrichs–Lewy (CFL) criterion as has been successfully used previously.<sup>22,23,33,34</sup>

The constitutive behavior is modeled using a large deformation isotropic viscoplastic flow rule based on Mises criterion, as detailed in previous works by Prakash *et al.*<sup>22,23</sup> The parameters for the power law viscoplastic constitutive model, Eq. (1), for HTPB, HMX, and the HTPB–HMX are given in Table I earlier. In order to capture the shock behavior, the Mie–Grüneisen equation of state is used to calculate the pressure  $p$  is given as<sup>22,35</sup>

$$p = K\phi + A\phi^2 + B\phi^3 + \gamma(1 + \phi)e, \quad (2)$$

where  $\phi = \frac{\rho}{\rho_0} - 1$ .

Here,  $K$  is the bulk modulus,  $A$  and  $B$  are parameters obtained from fitting a Hugoniot curve,<sup>35</sup>  $\gamma$  is the Grüneisen parameter,  $\rho_0$  is the initial density, and  $e$  is the internal energy per unit volume.

TABLE III. Mie–Grüneisen parameters for HTPB and HMX.

	$K$ ( $10^2$ GPa)	$A$ ( $10^2$ GPa)	$B$ ( $10^2$ GPa)	$\gamma$	$\rho_0$ ( $\text{g}/\text{cm}^3$ )	$E$ (MPa)	$\nu$
HTPB	0.02	0.294	0.0196	0.7	0.9	2.5	0.45
HMX	0.125	0.22	0.15	1.03	1.9	14240	0.31

The values of these parameters are given in Table III for HTPB<sup>35</sup> and HMX.<sup>36</sup>

A penalty based exponential relation between traction and separation is used to prevent interpenetration<sup>23,32</sup> during compressive loading. The temperature increase is calculated by  $\Delta T = T - T_{ref}$ , where  $T$  is the temperature in the current configuration, obtained from the equation of time rate of change of temperature given as<sup>37</sup>

$$\dot{T} = \frac{\dot{W}^{vp} + \dot{W}^f}{\rho c_p}, \quad (3)$$

where  $T_{ref}$  is taken to be equal to 298 K,  $W^{vp}$  is the plastic work,  $W^f$  is the heat generated due to friction between HTPB–HMX interfaces, and  $c_p$  is the heat capacity at constant pressure. The value for heat capacity for HTPB and HMX is taken to be equal to 2.5 kJ/(kg K)<sup>38</sup> and 0.97 kJ/(kg K),<sup>39</sup> respectively. The heat generated due to the frictional forces between bulk element surfaces is given by<sup>28</sup>

$$h = T \cdot \llbracket \mathbf{v} \rrbracket, \quad (4)$$

where  $h$  is the rate of heat generation. The surface traction,  $T$ , is acting between the bulk element surfaces, and  $\llbracket \mathbf{v} \rrbracket$  is the jump in the velocity of the corresponding surfaces. The generated heat is then distributed among the contacting bulk element surfaces using the method outlined by Camacho and Ortiz.<sup>28</sup>

### IV. RESULTS AND DISCUSSION

In order to observe the effect of microstructure on the failure properties and local temperature rise in HTPB/HMX based materials, 2D models of different microstructures with varying shapes and volume fraction of HMX particles were created as shown in



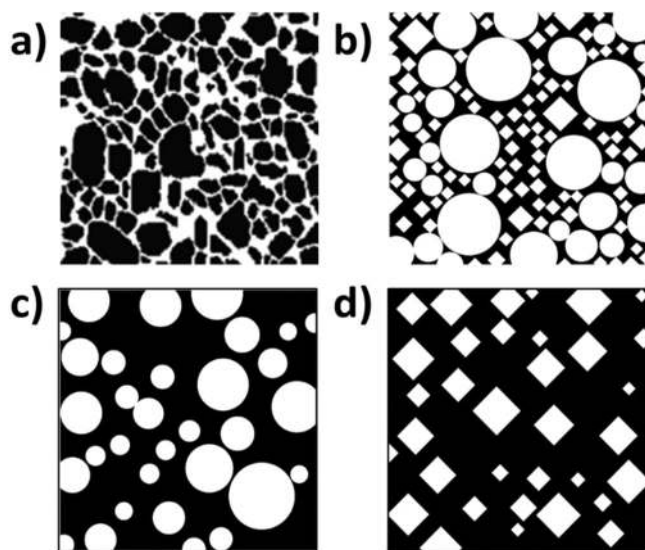


**FIG. 2.** Simulated microstructures of HTPB-HMX analyzed in this work. (a) Actual PBX microstructure (generated from work by Zhou *et al.*<sup>10</sup> is first simulated to compare with the literature findings, (b) microstructures with mixed smooth circular HMX particles and HMX particles with sharp edges, (c) microstructures with smooth circular HMX particles (varying densities), and (d) microstructures with HMX particles with sharp edges (varying densities).

Fig. 2. Earlier research has focused on modeling HMX single crystals accounting for orientation dependent crystal properties.<sup>49,50</sup> However, the experimental properties applied to this work were obtained for polycrystalline particles. Therefore, the HMX particles are modeled as polycrystalline  $\beta$ -HMX without orientation dependence. Crystal morphology plays a significant role in the behavior of an EM. Different grades of HMX may display different properties with respect to particle size and morphology. Detonator grade HMX has a crystal morphology that displays edges that are sharper while mil-spec HMX displays more rounded shapes.<sup>40</sup> A slight variation of crystal shape leads to different initiation characteristics, and the smoothing of material boundaries is known to reduce the shock sensitivity of the explosive.<sup>41</sup> In this work, we model microstructure with crystal shapes that represent the possible extremities in observed crystal morphology. Circular and diamond particles, in varying degrees of particle density, are generated to model the behavior of smooth and sharp particles, respectively, Fig. 2. A separate microstructure, generated using a combination of both types of particles with varying sizes, is also included to model the interaction between different particle shapes, Fig. 2(b). The circular particles had radii varying from  $100\ \mu\text{m}$  to  $300\ \mu\text{m}$ . The microstructures with diamond particles had approximately the same range of total volume fraction of EM particles as those with the circular EM particles.

Three different volume fractions, 40%, 60%, and 80% of the total volumes, of HMX particles, were considered. The PBX microstructure obtained from the literature is reported to have a 64% volume fraction of crystals.<sup>10</sup> For each microstructure-volume

fraction combination, simulations were also analyzed for different nominal strain rates. The range of microstructures based on literature morphology was chosen using methods outlined in earlier design studies<sup>42</sup> to cover a reasonable range. The nominal strain rate calculated in this work is the ratio of the impact velocity to the height of the sample. The current simulation framework has been experimentally validated under different loading conditions as well as varying strain rates from dynamic tensile to shock behavior of EMs in recent articles published by the authors.<sup>22,23,57</sup> It should be noted that the simulation framework in this work does not include frictional interaction after cohesive separation. This work is the first study on HTPB-HMX EMs with experimentally obtained properties. A detailed investigation of the deformation and temperature rise behavior of the HTPB-HMX PBX microstructure under an impact velocity of 300 m/s is presented in this work. The corresponding nominal strain rate is  $100\ 000\ \text{s}^{-1}$ . The impact condition was introduced by a velocity boundary condition at the top and bottom boundary as shown in Fig. 1(b) earlier. The left and right boundaries are kept traction free, as shown in Fig. 1.

### A. Application of the framework to the PBX microstructure reported in the literature by Liu *et al.*<sup>9</sup>

For comparison purposes, analyses were first performed on a digitized PBX microstructure taken from Barua and Zhou.<sup>10</sup> Pressure wave propagation in the literature PBX microstructure is shown through Figs. 3(a)–3(d). It is observed that the pressure wave does not propagate into the HMX phase and gets localized onto the HTPB-HMX interfaces, Figs. 3(a) and 3(b). As the value of the pressure increases, the intensity of the reflection also increases which creates a highly localized deformation near HTPB-HMX interfaces, Figs. 3(c) and 3(d). The pressure wave reflection at the HTPB-HMX interface also creates stress jump between HTPB and HMX phases leading to possible interface delamination. The wave velocity is approximately 5 km/s which is very close to what is reported in experimental studies (based on HTPB Hugoniot data by Millett *et al.*<sup>43</sup> and single crystal HMX Hugoniot data by Marsh<sup>44</sup> the upper and lower bounds for wave speeds in HTPB-HMX PBX are 5.977 km/s and 2.34 km/s, respectively).

The compressive stress change as a function of time, shown in Fig. 4, indicates higher stress concentration near the HTPB-HMX interfaces as time progresses. Initially, the stress is distributed throughout the HTPB binder phase, Fig. 4(a), and the HMX particles experience a lower stress level. However, as the wave propagates with time, the stress localization around HTPB-HMX interfaces increases and correspondingly the interaction between neighboring HMX particles also increases. Such an increase in particle interaction creates a higher concentration of stress at the HTPB-HMX interface. A further increase in the stress magnitude propagates the stress wave into the HMX particle. The wave reflects from the HMX particle boundary at HTPB-HMX interface and creates a lower level of tensile stress inside the particle.

The impact behavior of HTPB and HMX individually can be understood by analyzing the time dependent stress profiles in HTPB and HMX phases, as shown in Fig. 5. As observed in Figs. 5(a) and 5(d), the stress in the HTPB phase is considerably higher than that in the HMX phase. However, near the HTPB-HMX

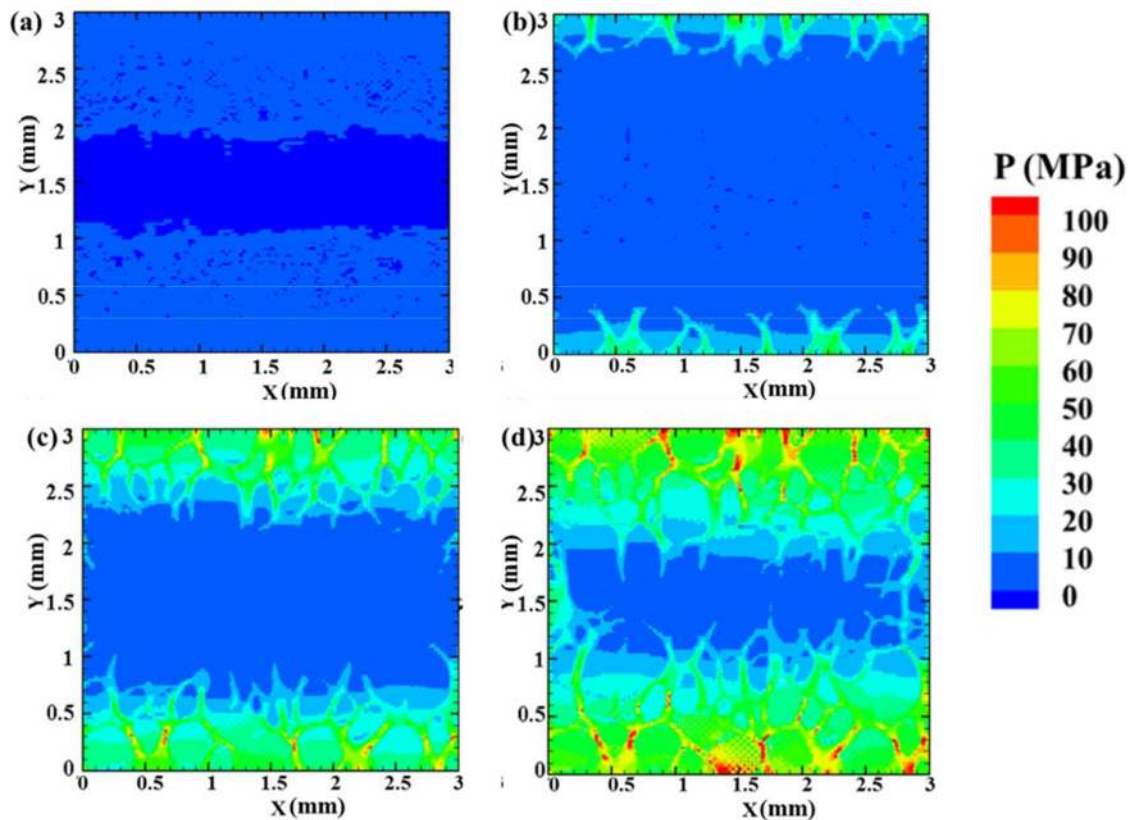


FIG. 3. Pressure distribution in the PBX microstructure at time: (a)  $0.2 \mu\text{s}$ , (b)  $0.4 \mu\text{s}$ , (c)  $0.6 \mu\text{s}$ , and (d)  $0.8 \mu\text{s}$ .

interfaces, the stress localization is high, Figs. 5(b) and 5(e). Although the stress inside large HMX particles remains low, the smaller HMX particles experience high stress, especially at the positions where particles are close to each other. This can be attributed to the relatively small area through which the stress waves travel before reflecting from the HTPB–HMX interfaces. A high level of interaction among the smaller HMX particles leads to high-stress concentration.

HTPB–HMX interface separation in the literature EM microstructure generates frictional heat dissipation. Shear stresses increase the possibility of interface fracture and subsequent frictional dissipation. As has been observed earlier by Needleman and Ortiz,<sup>45</sup> the interface boundary in a composite material acts as a barrier to shear waves. As shown in Fig. 6, shear stress in the vicinity of the HTPB–HMX interface is high as compared to the bulk HTPB and HMX phase and remains localized at the HTPB–HMX interfaces only. This increases the energy dissipation due to friction at the HTPB–HMX interface, which leads to an increase in temperature near such interfaces.

The viscoplastic dissipation is another factor that contributes to the increase in temperature. In this work, the viscoplastic dissipation dependent temperature rise is not separately modeled. That

remains a subject of ongoing experimental investigation. The distribution of effective viscoplastic strain within the PBX microstructure is plotted in Fig. 7 at different time steps to understand the role of viscoplastic dissipation. The viscoplastic strain in the HTPB phase is higher initially as compared to that in the HMX particles, Figs. 7(b) and 7(c), because of the higher stress and deformation observed in the HTPB phase. However, as time progresses, the viscoplastic strain near the HTPB–HMX interfaces increases and gets localized, Fig. 7(d). Such localization of viscoplastic strain increases the viscoplastic dissipation in this region that leads to an increase in the local temperature.

The EM microstructure failure under impact loading generates cracked surfaces that interact with the bulk phases and increase the frictional dissipation. In this work, a failure index *ICOHE* defined as the ratio of cohesive energy and the critical cohesive energy in a particular element is used for the understanding of damage propagation, Fig. 8. It is observed that the cohesive energy at the HTPB–HMX interfaces starts to increase first. This is due to the high-stress concentration and the stress difference between HTPB and HMX phases near the HTPB–HMX interface as was observed in Fig. 5 earlier as well. This is followed by HMX particle fracture at a high HMX volume fraction position due to high-stress concentration

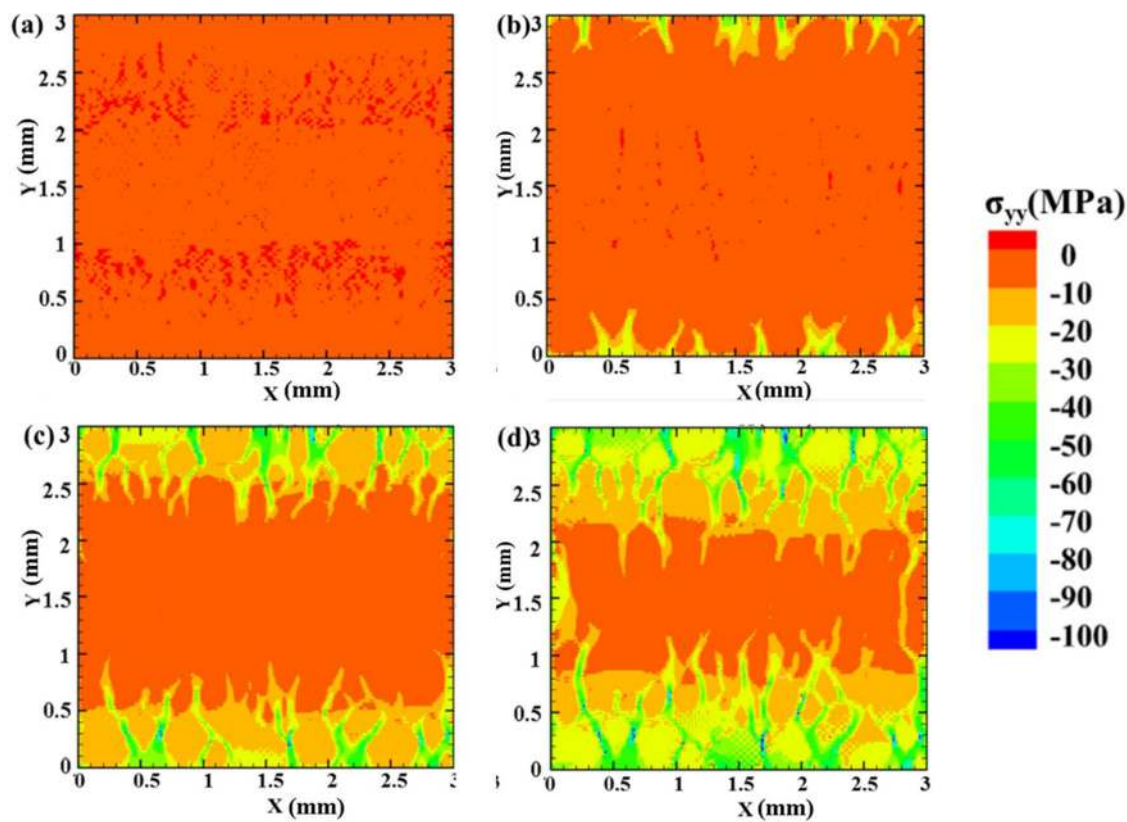


FIG. 4. Normal stress distribution in the PBX microstructure at time: (a)  $0.2 \mu\text{s}$ , (b)  $0.4 \mu\text{s}$ , (c)  $0.6 \mu\text{s}$ , and (d)  $0.8 \mu\text{s}$ .

and higher particle interaction at such regions as shown earlier in Fig. 4. Such failure behavior generates frictional dissipation that increases the temperature in these regions.

Figure 9 shows the temperature distribution in the literature PBX microstructure. The top and bottom boundary, where the constant velocity is applied, generates high temperature much earlier than that in the bulk due to the constant increase in pressure. Away from the boundary, a higher temperature is generated at the HTPB–HMX interface due to friction between particle and binder as well as between two or more particles. This has been experimentally observed in a recent article by Olokun *et al.*<sup>46</sup> as well. The temperature in the HMX phase is greater than the HTPB due to the higher stress and frictional dissipation due to particle fracture as was shown in Fig. 8. Temperature near the regions of high HMX volume fraction is higher than that near low HMX volume fraction regions. This is because of the increased interaction among particles as shown in Fig. 5.

In this work, the overall temperature rise behavior is described by the combined number of elements per unit area in the microstructure that reaches a temperature above a threshold value. The threshold temperature, in this case, is taken to be 400 K as suggested by Yang *et al.*<sup>47</sup> This number density can be taken to be a measure of hot-spot density. It has been shown by Kim *et al.*<sup>48</sup> that

the hot-spot temperature depends on the diameter of the hot-spot region selected. Figure 10(a) shows the hot-spot density as a function of threshold temperature. It can be observed that the hot-spot density, as well as the time rate of change of hot-spot density, decreases when the threshold temperature for hot-spot formation is increased. This means that there are fewer spots with higher temperature change and the number of such regions increases with time. A similar plot for the change in hot-spot density with time for increasing strain rate is shown in Fig. 10(b). The increase in strain rate increases the rate of stress and deformation within the microstructure which leads to an increase in the rate of change of hot-spot density.

## B. Comparison of literature microstructure results with idealized HMX particle shape based microstructures

The effect of HMX particle volume fraction and shape on the impact-induced failure behavior and temperature increase under impact loading is analyzed by understanding impact-induced failure behavior of idealized microstructures as shown in Fig. 2.

The volume-averaged compressive normal stress–strain behavior as a function of microstructure type (microstructures shown in Fig. 2) is shown in Fig. 11(a). It can be observed, from Fig. 11(a), that the microstructure with the diamond-shaped particles has a



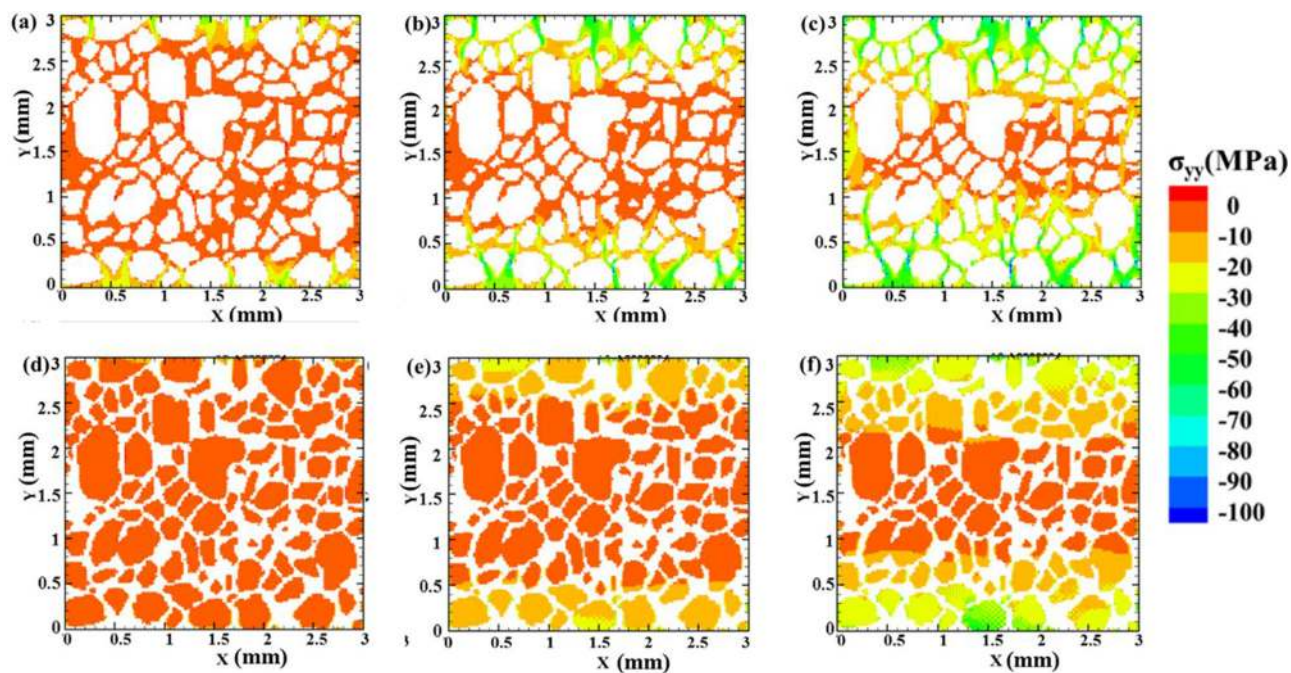


FIG. 5. Normal stress distribution in HTPB at time: (a)  $0.4 \mu\text{s}$ , (b)  $0.6 \mu\text{s}$ , and (c)  $0.8 \mu\text{s}$  and HMX at time: (d)  $0.4 \mu\text{s}$ , (e)  $0.6 \mu\text{s}$ , and (f)  $0.8 \mu\text{s}$ .

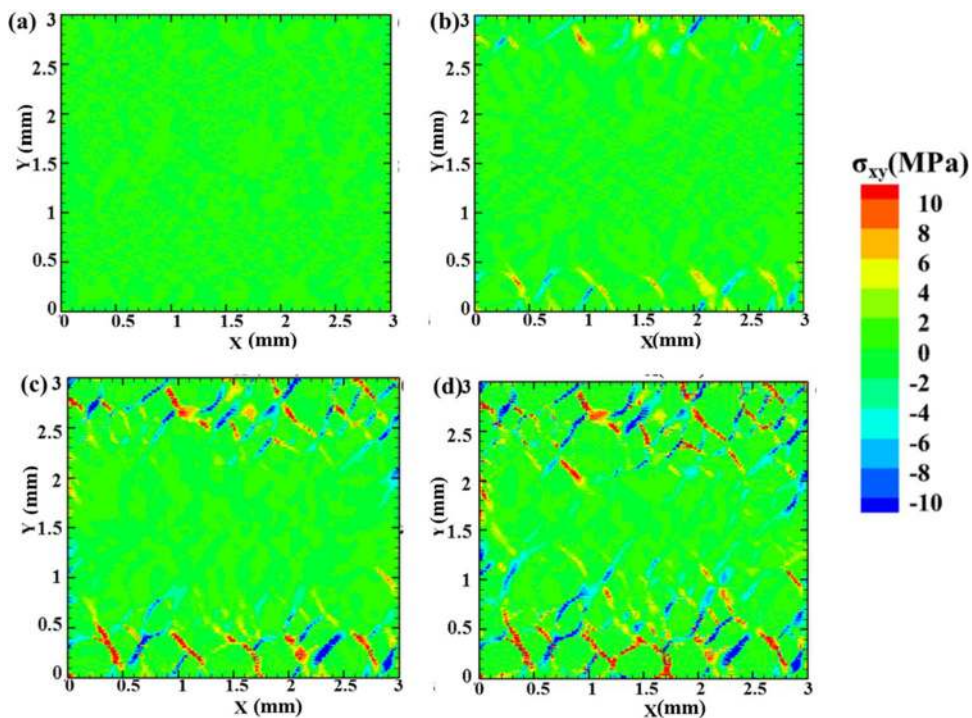


FIG. 6. Shear stress distribution in the PBX microstructure at time: (a)  $0.2 \mu\text{s}$ , (b)  $0.4 \mu\text{s}$ , (c)  $0.02 \mu\text{s}$ , and (d)  $0.8 \mu\text{s}$ .



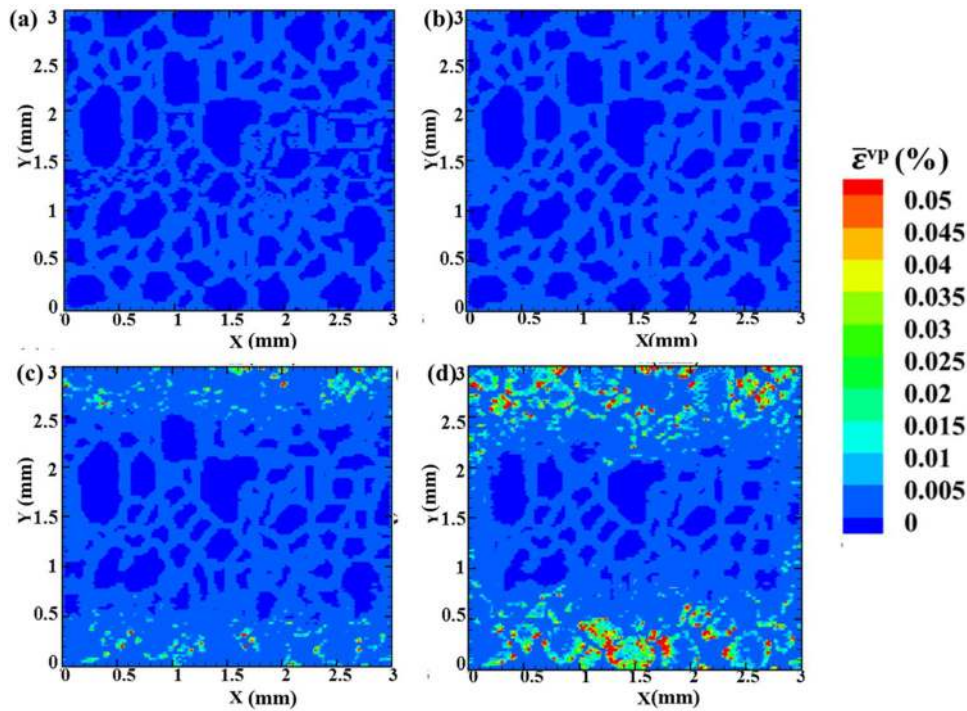


FIG. 7. Viscoplastic strain distribution in the PBX microstructure at time: (a) 0.2  $\mu\text{s}$ , (b) 0.4  $\mu\text{s}$ , (c) 0.6  $\mu\text{s}$ , and (d) 0.8  $\mu\text{s}$ .

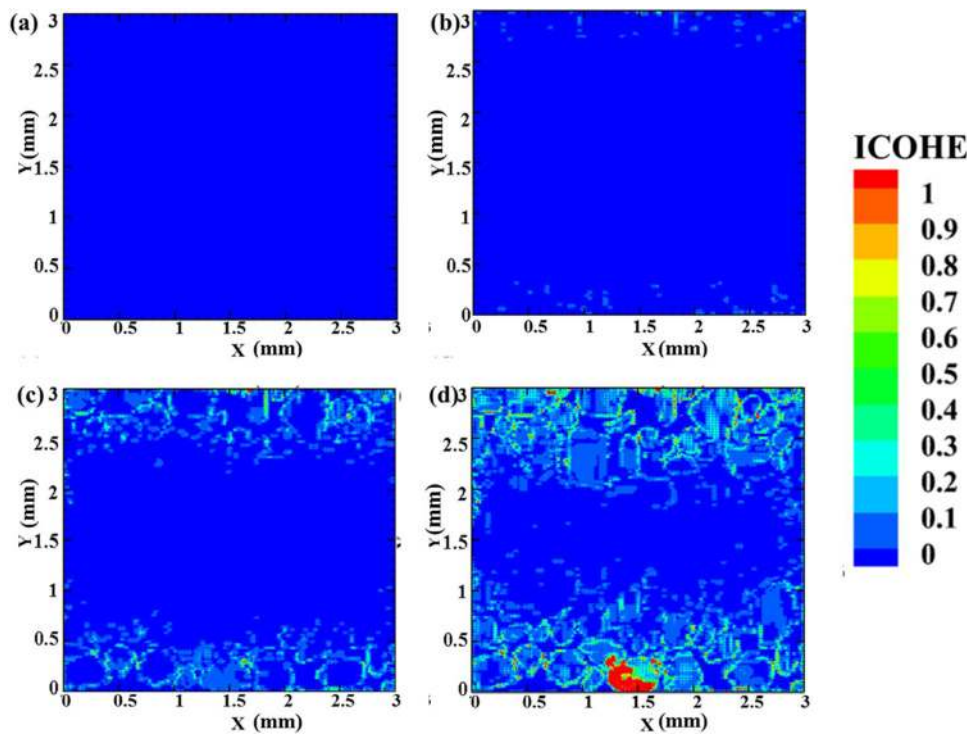


FIG. 8. Cohesive failure map in the PBX microstructure at time: (a) 0.2  $\mu\text{s}$ , (b) 0.4  $\mu\text{s}$ , (c) 0.6  $\mu\text{s}$ , and (d) 0.8  $\mu\text{s}$  (ICOHE is the ratio of cohesive energy and the critical cohesive energy).

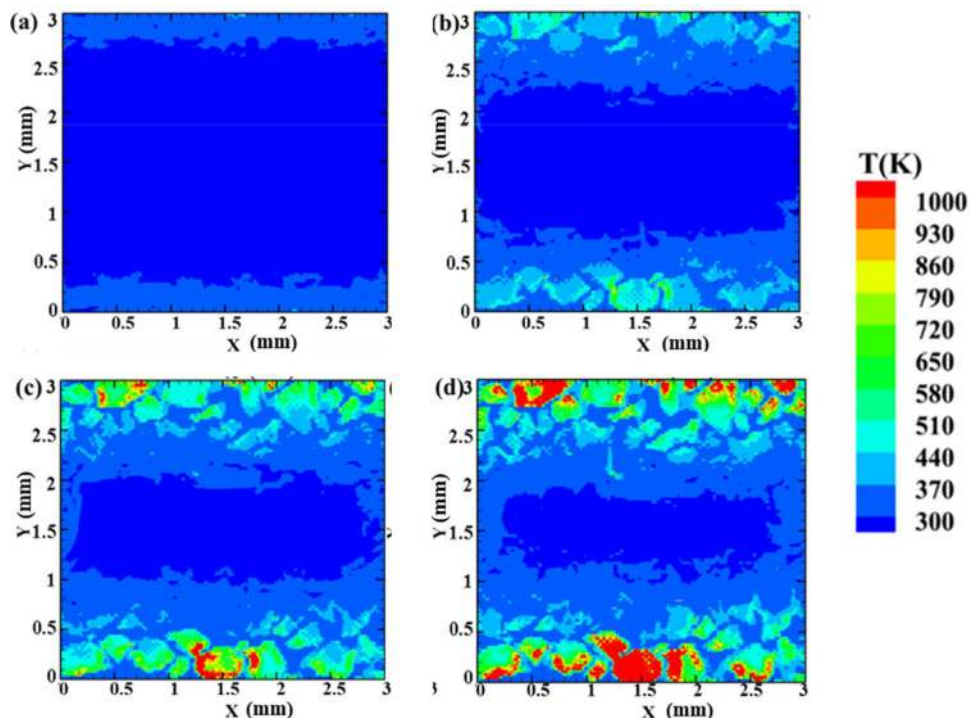


FIG. 9. Temperature distribution in the PBX microstructure at time: (a)  $0.4 \mu\text{s}$ , (b)  $0.6 \mu\text{s}$ , (c)  $0.7 \mu\text{s}$ , and (d)  $0.8 \mu\text{s}$ .

relatively lower stiffness that increases with an increase in particle volume fraction. This microstructure yields much earlier than the microstructures with other particle shapes generating a viscoplastic dissipation in the microstructure. This is expected and shown in the work of Baer,<sup>40</sup> where HMX crystals are modeled as both spherical and cubic particles. The works showed that the disorder

exhibited by the diamond particles due to orientation dependence will lead to the material exhibiting lower pressure fluctuations within the microstructure than the circular particles. It is also shown in Fig. 11(b) that the energy dissipation in the microstructure with diamond-shaped HMX particles is lower as compared to the other shapes. However, energy dissipation increases with an

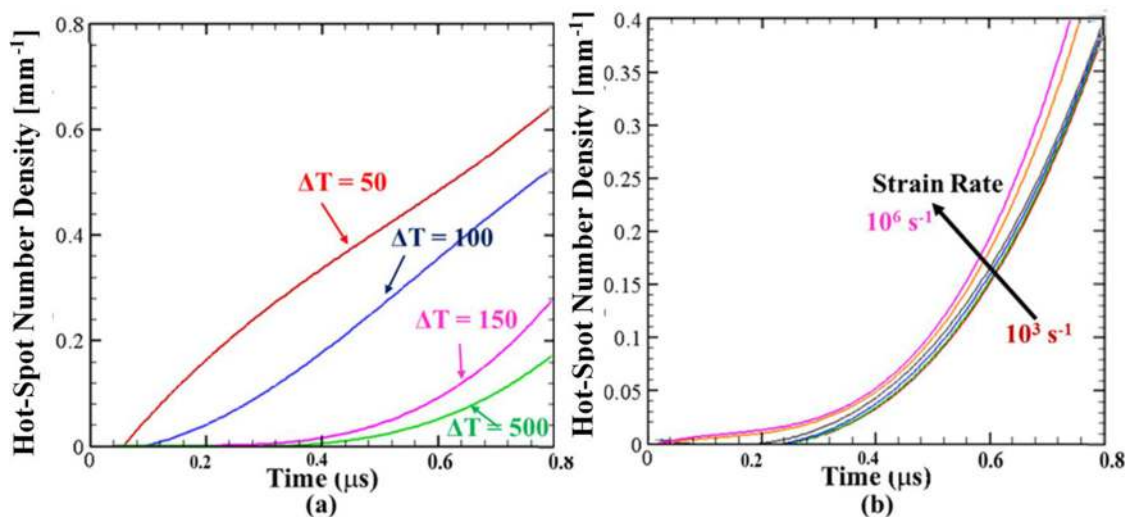


FIG. 10. Hot-spot density history in the PBX microstructure as a function of (a) threshold temperature change and (b) strain rate.

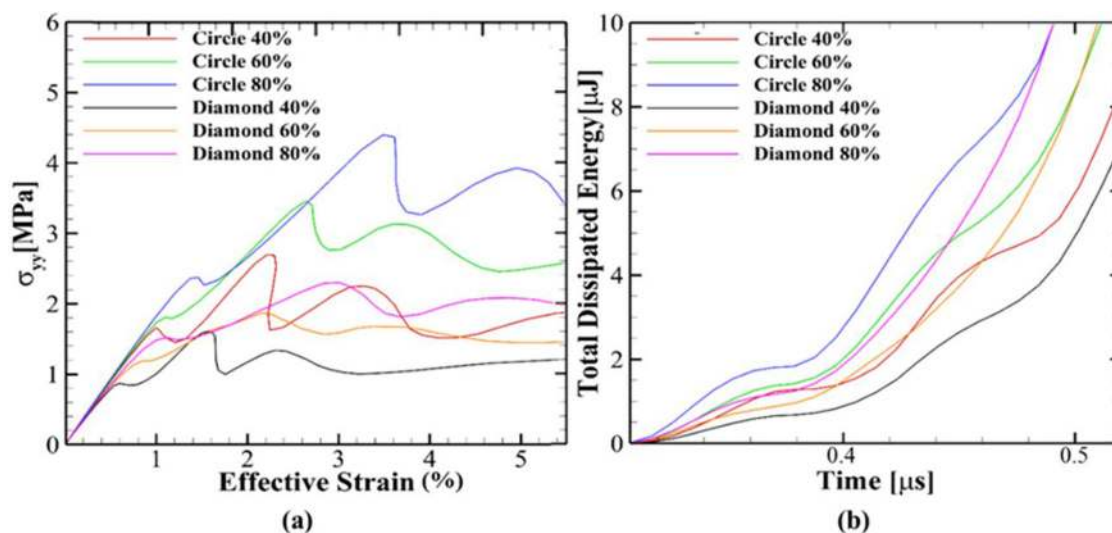


FIG. 11. (a) Normal stress vs effective strain and (b) total dissipation energy history as a function of HMX particle shape and volume fraction.

increase in particle volume fraction. This is expected as higher volume fraction creates a higher dynamic interaction between particles that generates higher stress concentration and deformation, as was observed in Figs. 6 and 7 as well.

In order to understand the effect of HMX shape on local temperature rise, the temperature profiles for the three microstructures with different shapes of the HMX particle along the centerline of the simulated sample ( $X = 1.5$  mm) are shown in Fig. 12. The

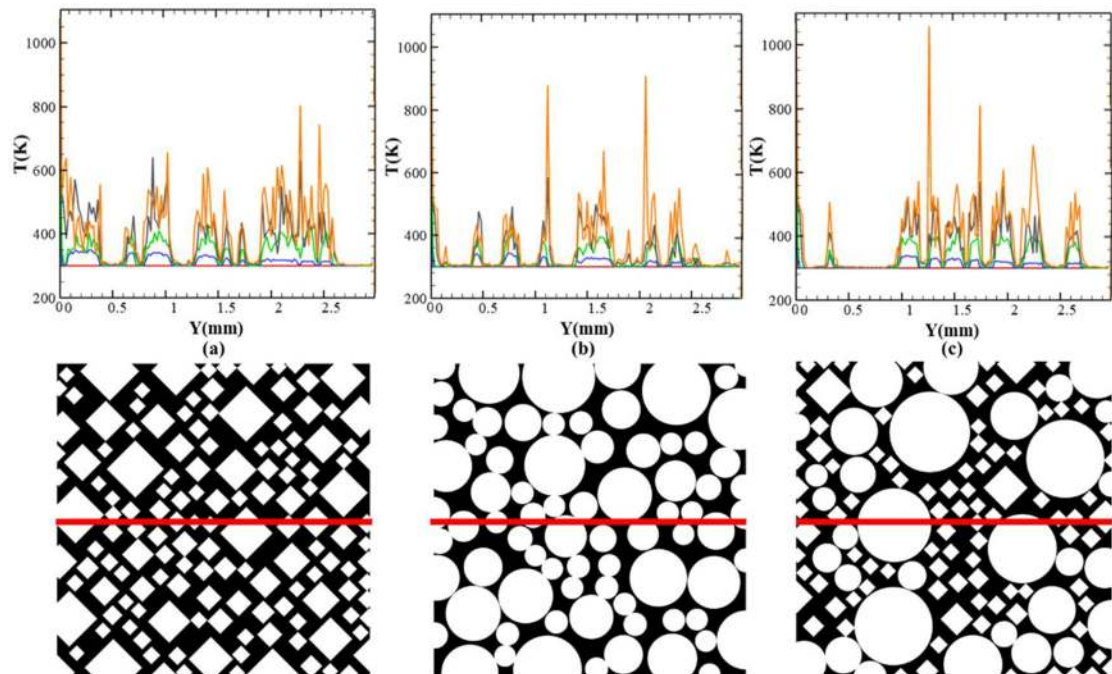


FIG. 12. Temperature profiles (top) along the centerline (bottom) of the 80% volume fraction microstructure with (a) diamond shaped, (b) circular shaped, and (c) mixed shaped HMX particles.



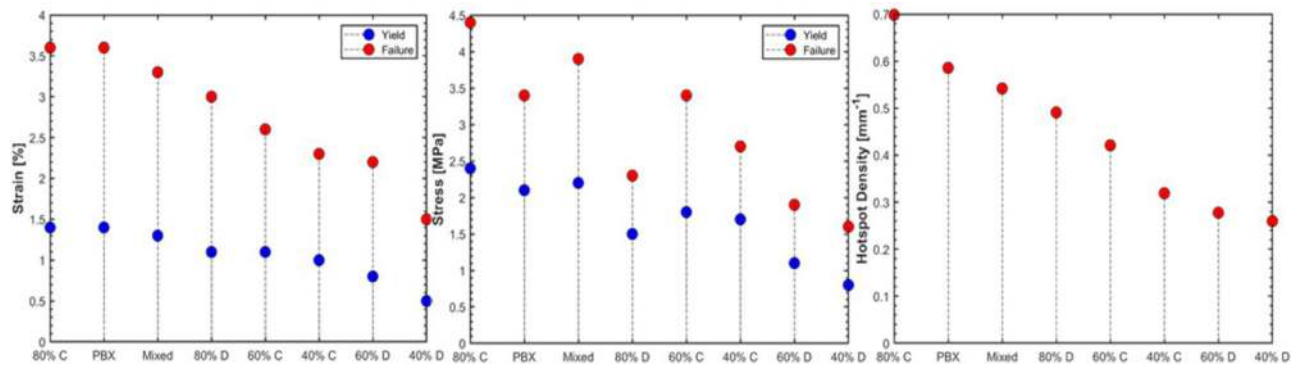


FIG. 13. Yield and failure (a) strain and (b) stress as a function of microstructure. (c) Hot-spot density as a function of the microstructure.

temperature is plotted as time progresses until the maximum temperature is reached. The progressive rise of temperature is shown at multiple time stamps with different colored lines. The comparison shows the areas close to the interfaces of larger HMX particles generate the highest impact-induced temperature. The maximum temperature in the microstructure with the circular particles is greater (950 K) than that in the microstructure with the diamond-shaped particles (800 K). The temperature farther from HTPB–HMX interfaces and inside particles was relatively lower. This is because the failure first starts at the HTPB–HMX interface that generates frictional dissipation combined with the higher viscoplastic dissipation. Higher viscoplastic dissipation is due to higher shear and normal stress concentration as well as high viscoplastic strain as was observed in Fig. 7. The maximum temperature rise achieved in this simulation can be compared to that reported by Kim *et al.*<sup>49</sup> where the maximum temperature was found to be about 800 K for HMX–Estane microstructure under moderate impact velocity ( $\sim 100$  m/s). However, Kim *et al.*<sup>49,50</sup> used a viscoelastic model for Estane and a viscoplastic constitutive model for the HMX. In this work, a strain-rate dependent viscoplastic model was used for both HTPB and HMX, which leads to an increase in heat dissipation leading to temperature increase. Higher temperatures around larger circular particles can be explained based on the size of particles. The circular particles have a larger surface area that lowers the yield strain<sup>8</sup> for interfaces modeled without friction in this work. In addition, microstructures with circular particles have a larger particle surface area in comparison to the microstructures with diamond-shaped particles for the same volume fraction. This feature dependence inherently gives circular microstructure a higher level of structural order leading to higher rigidity. Larger rigidity and lower yield strain combined with frictionless interfaces after separation lead to higher interaction level within particles in EM microstructures with circular particles in comparison to the EM microstructures with diamond-shaped particles. Similar size and shape dependent fracture issues have been observed in earlier studies in different material systems.<sup>51,52</sup>

The yield and failure properties for all analyzed microstructures (Fig. 2) with varying shapes and respective rigidity volume fractions are compared in Fig. 13. Figures 13(a) and 13(b) present

the yield and failure strains in descending order and show the highest volume fraction circular particle EM microstructure and the lowest volume fraction diamond particle EM microstructure to have the highest and lowest yield strains, respectively. It is observed that the highest and the lowest stress is exhibited by the same microstructure that had the highest and the lowest strains, respectively. A similar trend is shown in Fig. 13(c) for the impact-induced hot-spot density as a function of microstructure. The microstructure with higher volume fraction and circular-shaped particles has a higher affinity to show interface delamination. This increases the frictional dissipation energy leading to an increase in local temperature resulting in the temperature reaching the threshold temperature for the hot-spot formation. A similar effect has been demonstrated earlier using molecular simulations in other polymeric and polymer derived systems.<sup>53–56</sup>

## V. CONCLUSIONS

In this work, temperature rise and failure behavior of HTPB–HMX EM microstructure, under high-velocity impact, with different shapes and volume fractions of HMX particles were studied. The experimentally obtained strain-rate dependent viscoplastic model and interface separation properties were used to simulate impact behavior. It was observed that for all particle shapes, volume fraction, and strain rates, stress concentration at the HTPB–HMX interface was higher near the higher particle concentration, which increased the possibility of particle fracture in these regions. It was also observed that the microstructure with diamond-shaped (sharp corner) HMX had a lower stiffness and energy dissipation while the high-volume fraction microstructure with circular (smooth) HMX had the highest stiffness and energy dissipation. Microstructures with circular particles were found to be less resistant to fracture than the diamond-shaped HMX. Temperature maps showed that the HTPB–HMX interfaces are the critical regions where initiation may start in the absence of any other defect within the material. The microstructure with HMX particles in circular shape has a higher probability of temperature rise and hot-spot formation than microstructures with other particle shapes. Frictional heating combined with viscoplastic dissipation is found

to be mainly responsible for the local temperature rise in the regions with a high-volume fraction of HMX particles.

## ACKNOWLEDGMENTS

The authors gratefully acknowledge the financial support from the Air Force Office of Scientific Research, Dynamic Materials and Interactions Program (Grant No. FA9550-19-1-0318, Program Manager: Dr. Martin Schmidt).

## DATA AVAILABILITY

The data that support the findings of this study are available from the corresponding author upon reasonable request.

## REFERENCES

- <sup>1</sup>D. J. Benson and P. Conley, "Eulerian finite-element simulations of experimentally acquired HMX microstructures," *Model. Simul. Mater. Sci. Eng.* **7**(3), 333–354 (1999).
- <sup>2</sup>J. E. Field, "Hot spot ignition mechanisms for explosives," *Acc. Chem. Res.* **25**(11), 489–496 (1992).
- <sup>3</sup>J. G. Bennett, K. S. Haberman, J. N. Johnson, B. W. Asay, and B. F. Henson, "A constitutive model for the non-shock ignition and mechanical response of high explosives," *J. Mech. Phys. Solids* **46**(12), 2303–2322 (1998).
- <sup>4</sup>P. Rae, H. Goldrein, S. Palmer, J. Field, and A. Lewis, "Quasi-static studies of the deformation and failure of  $\beta$ -HMX based polymer bonded explosives," *Proc. R. Soc. A* **458**, 743 (2002).
- <sup>5</sup>S. Palmer, J. Field, and J. Huntley, "Deformation, strengths and strains to failure of polymer bonded explosives," *Proc. R. Soc. Lond. Ser. A* **440**, 399–419 (1993).
- <sup>6</sup>P. J. Rae, S. J. P. Palmer, H. T. Goldrein, J. E. Field, and A. L. Lewis, "Quasi-static studies of the deformation and failure of PBX 9501," *Proc. R. Soc. London. Ser. A* **458**(2025), 2227–2242 (2002).
- <sup>7</sup>C. Prakash, A. Olokun, I. Emre Gunduz, and V. Tomar, "Interface mechanical properties in energetic materials using nanoscale impact experiment and nano-mechanical Raman spectroscopy," in *Nano-Energetic Materials*, edited by S. Bhattacharya, A. K. Agarwal, T. Rajagopalan, and V. K. Patel (Springer Singapore, Singapore, 2019), pp. 275–290.
- <sup>8</sup>D. R. Drodge and W. G. Proud, "The effects of particle size and separation on PBX deformation," *AIP Conf. Proc.* **1195**(1), 1381–1384 (2009).
- <sup>9</sup>N. Liu, Y. Li, S. Zeman, Y. Shu, B. Wang, Y. Zhou, Q. Zhao, and W. Wang, "Crystal morphology of 3,4-bis(3-nitrofurazan-4-yl)furoxan (DNF) in a solvent system: Molecular dynamics simulation and sensitivity study," *CrystrEngComm* **18**(16), 2843–2851 (2016).
- <sup>10</sup>A. Barua and M. Zhou, "A Lagrangian framework for analyzing microstructural level response of polymer-bonded explosives," *Model. Simul. Mater. Sci. Eng.* **19**(5), 055001 (2011).
- <sup>11</sup>A. Barua, Y. Horie, and M. Zhou, "Microstructural level response of HMX-Estane polymer-bonded explosive under effects of transient stress waves," *Proc. R. Soc. A* **468**(2147), 3725–3744 (2012).
- <sup>12</sup>H. Tan, "The cohesive law of particle/binder interfaces in solid propellants," *Prog. Propul. Sci.* **2**, 59–66 (2011).
- <sup>13</sup>H. Tan, C. Liu, Y. Huang, and P. H. Geubelle, "The cohesive law for the particle/matrix interfaces in high explosives," *J. Mech. Phys. Solids* **53**(8), 1892–1917 (2005).
- <sup>14</sup>H. Tan, Y. Huang, C. Liu, and P. H. Geubelle, "The Mori-Tanaka method for composite materials with nonlinear interface debonding," *Int. J. Plast.* **21**(10), 1890–1918 (2005).
- <sup>15</sup>H. Tan, Y. Huang, and C. Liu, "The viscoelastic composite with interface debonding," *Compos. Sci. Technol.* **68**(15), 3145–3149 (2008).
- <sup>16</sup>A. Barua, Y. Horie, and M. Zhou, "Energy localization in HMX-Estane polymer-bonded explosives during impact loading," *J. Appl. Phys.* **111**(5), 054902 (2012).
- <sup>17</sup>A. Barua, S. P. Kim, Y. Horie, and M. Zhou, "Computational analysis of ignition in heterogeneous energetic materials," *Mater. Sci. Forum* **767**, 13–21 (2013).
- <sup>18</sup>B. Koohbor, S. Ravindran, and A. Kidane, "Experimental study of the meso-scale heterogeneous deformation response of polymer composites," in *Proceedings of the American Society for Composites 30th Technical Conference* (DEStech Publications, Inc., Lancaster, PA, 2015), Vol. 30, p. 1369.
- <sup>19</sup>S. Ravindran and A. Kidane, "Meso-scale deformation behavior of polymer bonded energetic material under quasi-static compression," in *Mechanics of Composite and Multi-Functional Materials* (Springer, Cham, 2016), Vol. 7, pp. 345–350.
- <sup>20</sup>S. Ravindran, B. Koohbor, and A. Kidane, "Experimental investigation of compaction wave propagation in cellular polymers," in *International Digital Imaging Correlation Society. Conference Proceedings of the Society for Experimental Mechanics Series*, edited by M. Sutton and P. Reu (Springer, Cham, 2017), pp. 113–115.
- <sup>21</sup>S. Ravindran, A. Tessema, and A. Kidane, "Effect of crystal density on dynamic deformation behavior of PBX," in *Challenges in Mechanics of Time Dependent Materials* (Springer, Cham, 2017), Vol. 2, pp. 87–92.
- <sup>22</sup>C. Prakash, I. E. Gunduz, and V. Tomar, "Simulation guided experimental interface shock viscosity measurement in an energetic material," *Model. Simul. Mater. Sci. Eng.* **27**(8), 085003 (2019).
- <sup>23</sup>C. Prakash, I. E. Gunduz, C. Oskay, and V. Tomar, "Effect of interface chemistry and strain rate on particle-matrix delamination in an energetic material," *Eng. Fract. Mech.* **191**, 46–64 (2018).
- <sup>24</sup>D. Verma, M. Exner, and V. Tomar, "An investigation into strain rate dependent constitutive properties of a sandwiched epoxy interface," *Mater. Design* **112**, 345–356 (2016).
- <sup>25</sup>A. Olokun, C. Prakash, I. Emre Gunduz, and V. Tomar, "Interface chemistry dependent mechanical properties in energetic materials using nano-scale impact experiment," in *Dynamic Behavior of Materials*, edited by J. Kimberley, L. Lamberson, and S. Mates (Springer, Cham, 2019), Vol. 1, pp. 147–152.
- <sup>26</sup>C. Prakash, I. Emre Gunduz, and V. Tomar, "Effect of strain rate and interface chemistry on failure in energetic materials," in *Fracture, Fatigue, Failure and Damage Evolution, Conference Proceedings of the Society for Experimental Mechanics Series*, edited by J. Carroll, S. Xia, A. Beese, R. Berke, and G. Pataky (Springer, Cham, 2018), Vol. 7, pp. 7–12.
- <sup>27</sup>V. Tomar and M. Zhou, "Deterministic and stochastic analyses of fracture processes in a brittle microstructure system," *Eng. Fract. Mech.* **72**(12), 1920–1941 (2005).
- <sup>28</sup>G. T. Camacho and M. Ortiz, "Computational modelling of impact damage in brittle materials," *Int. J. Solids Struct.* **33**(20), 2899–2938 (1996).
- <sup>29</sup>M. Ortiz and A. Pandolfi, "Finite-deformation irreversible cohesive elements for three-dimensional crack-propagation analysis," *Int. J. Numer. Meth. Eng.* **44**(9), 1267–1282 (1999).
- <sup>30</sup>H. Tan, Y. Huang, and P. Geubelle, "An energy approach to a micromechanics model accounting for nonlinear interface debonding," in *41st AIAA/ASME/SAE/ASEE Joint Propulsion Conference & Exhibit* (American Institute of Aeronautics and Astronautics, 2005), Paper No. AIAA 2005-3995.
- <sup>31</sup>V. Tomar, "Modeling of dynamic fracture and damage in two-dimensional trabecular bone microstructures using the cohesive finite element method," *J. Biomech. Eng.* **130**(2), 021021 (2008).
- <sup>32</sup>V. Tomar, "Analyses of the role of the second phase SiC particles in microstructure dependent fracture resistance variation of SiC-Si<sub>3</sub>N<sub>4</sub> nanocomposites," *Model. Simul. Mater. Sci. Eng.* **16**(3), 035001 (2008).
- <sup>33</sup>V. Tomar, J. Zhai, and M. Zhou, "Bounds for element size in a variable stiffness cohesive finite element model," *Int. J. Numer. Meth. Eng.* **61**(11), 1894–1920 (2004).
- <sup>34</sup>J. Zhai, V. Tomar, and M. Zhou, "Micromechanical simulation of dynamic fracture using the cohesive finite element method," *J. Eng. Mater. Technol.* **126**(2), 179–191 (2004).
- <sup>35</sup>J. E. Reaugh and E. L. Lee, "Shock Hugoniot behavior of mixed phases with widely varying shock impedances," in *Shock Compression of Condensed Matter -1997*, edited by S. C. Schmidt, D. P. Dandekar, and J. W. Forbes (1998), available at <https://www.osti.gov/servlets/purl/633089>.

- <sup>36</sup>A. Pi, F. Huang, Y. Wu, and Z. Zhang, "Anisotropic constitutive model and numerical simulations for crystalline energetic material under shock loading," *Math. Mech. Solids* **19**(6), 640–658 (2014).
- <sup>37</sup>J. Clayton, "Modeling and simulation of ballistic penetration of ceramic-polymer-metal layered systems," *Math. Probl. Eng.* **2015**, 1–10 (2015).
- <sup>38</sup>F. R. Chaves and J. C. Góis, "Research on the specific heat capacity of PBX formulations based on RDX," *J. Aerosp. Technol. Manag.* **8**(3), 352–356 (2016).
- <sup>39</sup>J. F. Baytos, *LASL Explosive Property Data* (Los Alamos Scientific Laboratory, 1967).
- <sup>40</sup>M. R. Baer, "Modeling heterogeneous energetic materials at the mesoscale," *Thermochim. Acta* **384**(1), 351–367 (2002).
- <sup>41</sup>A. C. V. D. Steen, H. J. Verbeek, and J. J. Meulenbrugge, "Influence of RDX crystal shape on the shock sensitivity of PBXs," in *Proceedings of the 9th Symposium (International) on Detonation, Portland, OR* (Naval Surface Warfare Center, Silver Spring, MD, 1989), p. 83.
- <sup>42</sup>G. Mejía-Rodríguez, J. E. Renaud, and V. Tomar, "A variable fidelity model management framework for designing multiphase materials," *ASME. J. Mech. Des.* **130**(9), 091702 (2008).
- <sup>43</sup>J. C. F. Millett, N. K. Bourne, and J. Akhavan, "The response of hydroxy-terminated polybutadiene to one-dimensional shock loading," *J. Appl. Phys.* **95**(9), 4722–4727 (2004).
- <sup>44</sup>S. P. Marsh, *LASL Shock Hugoniot Data* (University of California Press, 1980), Vol. 5.
- <sup>45</sup>A. Needleman and M. Ortiz, "Effect of boundaries and interfaces on shear-band localization," *Int. J. Solids Struct.* **28**(7), 859–877 (1991).
- <sup>46</sup>A. Olokun, B. Li, C. Prakash, Z. Men, D. D. Dlott, and V. Tomar, "Examination of local microscale-microsecond temperature rise in HMX-HTPB energetic material under impact loading," *J. Mater.* **71**(10), 3531–3535 (2019).
- <sup>47</sup>K. Yang, Y. Wu, and F. Huang, "Numerical simulations of microcrack-related damage and ignition behavior of mild-impacted polymer bonded explosives," *J. Hazard. Mater.* **356**, 34–52 (2018).
- <sup>48</sup>S. Kim, C. Miller, Y. Horie, C. Molek, E. Welle, and M. Zhou, "Publisher's note: "Computational prediction of probabilistic ignition threshold of pressed granular octahydro-1,3,5,7-tetranitro-1,3,5,7-tetrazocine (HMX) under shock loading" *J. Appl. Phys.* **120**, 115902 (2016)," *J. Appl. Phys.* **120**(18), 189901 (2016).
- <sup>49</sup>S. Kim, A. Barua, Y. Horie, and M. Zhou, "Ignition probability of polymer-bonded explosives accounting for multiple sources of material stochasticity," *J. Appl. Phys.* **115**(17), 174902 (2014).
- <sup>50</sup>S. Kim, Y. Horie, and M. Zhou, "Ignition desensitization of PBX via aluminization," *Metal. Mater. Trans. A* **46**(10), 4578–4586 (2015).
- <sup>51</sup>C. Prakash, H. Lee, and M. Alucozai, "An analysis of the influence of grain boundary strength on microstructure dependent fracture in polycrystalline tungsten," *Int. J. Fract.* **199**(1), 1–20 (2016).
- <sup>52</sup>Y. Han and V. Tomar, "An ab initio study of the peak tensile strength of tungsten with an account of helium point defects," *Int. J. Plast.* **48**, 54–71 (2013).
- <sup>53</sup>T. Qu, D. Verma, M. Alucozai, and V. Tomar, "Influence of interfacial interactions on deformation mechanism and interface viscosity in  $\alpha$ -chitin-calcite interfaces," *Acta Biomater.* **25**, 325–338 (2015).
- <sup>54</sup>D. Dubey and V. Tomar, "Microstructure dependent dynamic fracture analyses of trabecular bone based on nascent bone atomistic simulations," *Mech. Res. Commun.* **35**(1–2), 24–31 (2008).
- <sup>55</sup>D. K. Dubey and V. Tomar, "The effect of tensile and compressive loading on the hierarchical strength of idealized tropocollagen-hydroxyapatite biomaterials as a function of the chemical environment," *J. Phys. Condens. Matter* **21**(20), 205103 (2009).
- <sup>56</sup>V. Tomar, M. Gan, and H. S. Kim, "Atomistic analyses of the effect of temperature and morphology on mechanical strength of Si–C–N and Si–C–O nanocomposites," *J. Eur. Ceram. Soc.* **30**(11), 2223–2237 (2010).
- <sup>57</sup>C. Prakash, I. E. Gunduz, and V. Tomar, "The effect of interface shock viscosity on the strain rate induced temperature rise in an energetic material analyzed using the cohesive finite element method," *Modell. Sim. Mater. Sci. Eng.* **27**(6), 065008 (2019).